https://doi.org/10.5194/nhess-2020-120
Preprint. Discussion started: 20 April 2020

Natural Hazards and Earth System Sciences
Open Access
Discussions

Assimilation of Himawari-8 Imager Radiance Data with the WRF-3DVAR system for the prediction of Typhoon Soulder

Dongmei Xu[1,2*], Aiqing Shu[1], Zhankui Zhang[1]

1. *the Key Laboratory of Meteorological Disaster, Ministry of Education (KLME)/Joint International Research Laboratory of Climate and Environment Change (ILCEC)/Collaborative Innovation Center on Forecast and Evaluation of Meteorological Disasters (CIC-FEMD), Nanjing University of Information Science & Technology, Nanjing 210044, China*
2. *Heavy Rain and Drought-Flood Disasters in Plateau and Basin Key Laboratory of Sichuan Province, Chengdu, China*

https://doi.org/10.5194/nhess-2020-120
Preprint. Discussion started: 20 April 2020

Abstract

Himawari-8 is a new generation geostationary meteorological satellite launched by Japan Meteorological Agency (JMA). It carries the Advanced Himawari imager (AHI) onboard, which can continuously monitor high-impact weather events with high frequency space and time. The assimilation of AHI was implemented with the framework of the mesoscale numerical model WRF and its three-dimensional variational assimilation system (3DVAR) for the analysis and prediction of typhoon "Soudelor" in the Pacific Typhoon season in 2015. The effective assimilation of AHI Imager data in tropical cyclone with rapid intensify development has been realized. The results show that after assimilating the AHI imager data under clear sky conditions, the typhoon position in the background field in the model is effectively corrected compared with the control experiment without AHI data. It is found that assimilation of AHI imager data is able to improve the analyses of the water vapor and wind in typhoon inner-core region. The analyses and forecast of the typhoon minimum sea level pressure, the maximum near-surface wind speed, and the typhoon track are further improved.

Key words: Weather Research and Forecasting model; Three-Dimensional Variational Data Assimilation; AHI Imager Data; Typhoon

https://doi.org/10.5194/nhess-2020-120
Preprint. Discussion started: 20 April 2020

Natural Hazards and Earth System Sciences Discussions

1. Introduction

In recent years, although researchers have made great progress in the field of NWP (numerical weather prediction), the huge challenges are encountered in the exact forecast of tropical cyclones (TCs) with quick intensifications (DeMaria et al., 2014). The predictability of these TCs is limited because it entails complex multi-scale dynamic interactions. These interactions include environmental airflows, TC vortex interactions, atmosphere-ocean interactions, and the effects of mesoscale and micro-convective scale, together with microphysics and atmospheric radiation. In order to attain a better initial condition (IC) and improve the accuracy of forecast, data assimilation seeks to fully utilize the observations. Most of TC's life span is over the ocean where conventional observations are relatively limited. Therefore, by analyzing observed data from the satellites and planes over the sea, it is crucial to adopt effective data assimilation (DA) methods to improve the analysis and forecast of TCs.

With the rapid development of atmospheric radiative transfer model (RTM), many numerical forecast centers now can adopt variational DA method to assimilate a variety of radiance data from different satellite observation instruments directly (Bauer et al., 2011; Buehner et al., 2016; Derber et al., 1998; Hilton et al., 2009; Kazumori et al., 2014; McNally et al., 2006; Prunet et al., 2000; Pennie, 2010). These data can take up 90% of all data used in global DA system and can improve NWP technique strikingly (Bauer et al., 2010). Some related researches demonstrated that in global model, satellite radiance DA makes more contributions to forecast accuracy

https://doi.org/10.5194/nhess-2020-120
Preprint. Discussion started: 20 April 2020

Natural Hazards and Earth System Sciences
Discussions

than conventional observation DA (Zapotocny et al., 2007).

Generally speaking, radiance data is derived from microwave and infrared detecting instruments, which are from polar-orbit satellites and geostationary satellites, respectively. Polar-orbit satellites cover the sphere of all the earth, so their observations are suitable for global numerical forecast models (Jung et al., 2008). Besides, compared to geostationary satellites, they have higher resolutions (Li et al., 2017; Shen et al., 2015; Xu et al., 2013). However, it is highlighted that they are not able to perform continuous observation over a fixed area, so this can leave out some quickly intensified TCs or storms. On the contrary, because geostationary satellites have a fixed location related to the earth's surface, although their resolutions are lower than polar-orbit satellites, they can capture the formation and development of mesoscale systems by continuous monitoring (Montmerle et al., 2007; Stengel et al., 2009; Zou et al.,2011).

Geostationary satellites are able to continuously detect a region at a higher frequency, thus supervising TCs over the vast ocean effectively. In fact, they can capture convective spiral cloud systems relating to TCs and act as an important role in TC's optimum observational position. As the first new generational geostationary satellite, Himawari-8 was launched successfully in Sep 2014 by JMA (Japan Meteorological Agency) and put into operation in July 2015 (Bessho et al., 2016). It has an advanced imager called AHI (Advanced Himawari Imager) with 16 visible and infrared bands, including 3 moisture channels, which can conduct a full-disk scan

https://doi.org/10.5194/nhess-2020-120
Preprint. Discussion started: 20 April 2020

every 10 minutes. Meanwhile, it can also acquire regional scan images and that is to say it can scan the Japan and the target areas every 2.5 minutes. Compared to the early geosynchronous imagers, AHI has more spectrum bands and this can monitor the state of atmosphere with a higher frequency.

In recent years, some experts and scholars have carried out some researches on geostationary satellite observation DA. Firstly utilizing GSI (Gridpoint Statistical Interpolation) from NCEP (National Centers for Environmental Prediction), Zou, et al (2011) conducted direct assimilation on imagers' data from GOES-11 and GOES-12 to estimate their potential influences on QPF (quantitative precipitation forecasts) of coastal regions in the eastern part of American. They found assimilating radiance data from GOES's imager has a remarkable improvement on 6 to 12 hour's QPF near northern Mexico Gulf coast. Their work was continued by Qin, et al (2013), which put thinned radiance data into GSI assimilation system to make a comprehensive investigation on the issue on combined assimilation of GOES Imager data together with AMSU-A (Advance Microwave Sounding Unit-A), AMSU-B (Advance Microwave Sounding Unit-B), AIRS, MHS (Microwave Humidity Sounder), HIRS (High Resolution Infrared Radiation Sounder), GSN (GOES Sounder). The results showed the effect of single assimilation of AHI data is better than combined assimilation in term of precipitation forecast. Zou, et al (2015) adopted GSI system to assimilate radiance data from four infrared channels on GOES-13/15 and set up two experiments for comparison. A symmetric vortex was used for initialization in the first

https://doi.org/10.5194/nhess-2020-120
Preprint. Discussion started: 20 April 2020

trial and an asymmetric counterpart for the other trial. Results showed that direct assimilation of GOES-13/15's radiance data could generate continuous positive effects on the track and intensity forecasts of tropical storm "Debbie" and this impact was derived from assimilation of GOES radiance along with asymmetric vortex initialization. Because himawari-8 has not been in operation for a long time, there are few studies on himawari-8 data. Ma, et al (2017) used 4DEnVar (4D ensemble variational data assimilation) in NCEP's GSI system to assimilate radiance of three moisture channels of AHI under clear-sky condition and then NCEP GFS (Global Forecast System) was utilized to estimate the impacts of AHI assimilation on whether analysis and forecast. They found it had a positive influence on the forecast of global vapor at high level of troposphere. Wang, et al (2018), based on 3DVAR system in NWP center in northeast China operated by Liaoning Meteorological Bureau, firstly attempted to conduct convective scale assimilation of AHI three moisture channels' radiance data to study its impacts on the analysis and forecast of a rainstorm in Northern China on 19th of Sep. It turned out that the assimilation of AHI radiance could improve the simulated wind and vapor fields and the accuracy of rainfall forecast in the first 6 hours obviously.

Although former researches have made several achievements in satellite data assimilation and application, it is still a challenge to make more effective use of the new generational geostationary satellite imager data with high spatial and temporal resolution so that it can better satisfy the needs of meteorology. In most previous studies, researches usually use a 6 hour's or even longer time interval with a coarse spatial resolution. Therefore, until now hourly fast updating assimilation technique of the stationary satellite radiance data in the convective scale in term of the analyses and prediction of tropical cyclones has not been well carried out. This paper intends to employ the new generational mesoscale WRF model and build an assimilation system aimed at AHI imager data. Then a case of typhoon Soudelor is studied by performing numerical simulation to address the impacts of convective assimilation on the improvement of TC's IC and the enhancement of TC's track and intensity forecast.

2. Observational data and DA system

2.1 An introduction to Himawari-8 AHI radiance data

Himawari-8 satellite was launched by JMA (Japan Meteorological Agency) to a geosynchronous orbit on 17 October 2014 and has begun its operational use since 7 July 2015. It is the first satellite of all new generational geosynchronous meteorological satellites and plays a pioneering role for the geosynchronous imagers to be launched in US, China, Korea and Europe. Himawari-8 is located between the equator and 140.7°E, so the earth is observed between 60°N and 60°S meridionally and between 80°E and 160°W zonally. Compared to its previous generation Himawari-7, its detective ability can get remarkably improved since the instrument AHI on Himawari-8. Besides, its device is comparable to imagers on American GOES-R satellite (Goodman et al., 2012; Schmit et al., 2005; Schmit et al., 2008; Schmit et al., 2017). AHI is able to provide a full-disk image every 10 minutes and

https://doi.org/10.5194/nhess-2020-120
Preprint. Discussion started: 20 April 2020

complete a scan over Japan every 2.5 minutes. AHI conducts continuous scan and detection on a moving targeted typhoon. It has 16 channels covering visible, near-infrared, and infrared spectral bands with a resolution of 0.5 km or 1 km, 0.5 km or 1 km, and 2 km respectively. Channel 8 to 10 (6.2, 6.9, and 7.3 μm) are water vapor bands that are sensitive to the humidity in the middle and upper troposphere (Di et al., 2016). Other channels (channel 11, 12, 16: 8.6 μm, 9.6 μm, and 13.3μm) are either monitoring other fields such as the thin ice clouds, volcanic SO2 gas, the ozone or CO2, or the atmospheric window channels (13-15: 10.4, 11.2, and 12.4 μm) function as monitors for ice crystal/water, low water vapor, volcanic ash, SST (Sea Surface Temperature) and other phenomena (Bessho et al., 2016).

Our work focuses mainly on assimilating the three moisture channels (6.2, 6.9, and 7.3μm) since they are very sensitive to the humidity in the middle and upper troposphere and have a certain effect on the lower troposphere. Thus, a large amount of effective atmospheric information can be provided for AHI radiance data assimilation in the troposphere.

2.2 WRFDA system and AHI assimilation module

WRFDA system is designed by National Center for Atmospheric Research (NCAR) and it contains 3DVAR, 4DVAR, Hybrid parts. Our research is based on the 3DVAR method. An interface that is suitable for AHI DA is built in WRFDA system. Currently, WRFDA is able to assimilate many conventional and unconventional observation. In terms of satellite radiance observation, this system is compatible with RTTOV (the Radiative Transfer model of the Television and Infrared Observational

https://doi.org/10.5194/nhess-2020-120
Preprint. Discussion started: 20 April 2020

Satellite (TIROS) Operational Vertical sounder) and CRTM (Community Radiative Transfer Model) as observational operators. In this paper, CRTM is utilized as the observational operator to simulate and compute AHI radiance data. Estimating the systematic bias and random error of the observation data caused by the errors of numerical models and instruments is the key to directly assimilate the satellite radiance data. Apart from eliminating cloud pixels, other procedures to conduct quality control are as follows. (1) when reading the data, remove the observed outliers with the observed values below 50 K or above 550 K; (2) only the marine observations are applied by removing the observation on the land and the more complex observation points on the ocean surface; (3) remove observations when the observation minus the background simulation is larger than 3 times of the observation error; (4) the pixel point is removed when the CLW calculated by the background field of the numerical model is greater than or equal to 0.2 kg/m2; (5) eliminate the data when the observed value minus the background simulation value is greater than 5 K; (6) only vapor channels 8, 9, 10 on AHI are assimilated (Wang et al., 2018).

By using 3DVar algorithm, the assumption is that there is no bias between observation and background (Dee et al., 2009; Liu et al., 2012; Zhu et al., 2014). A bias correction scheme for observation is essential before DA. Usually, radiance bias can be obtained by a linear combination of a set of forward operators.

$$\tilde{H}(x,\beta)=H(x)+\beta_0+\sum_{i=1}^{N_p}\beta_i p_i \qquad (1)$$

Here, $H(x)$ represents the initial observation operator (before the bias correction), x represents the mode state vector, β_0 represents a constant component of the total bias (constant part), p_i and β_i represent the i-th predictor and its coefficient respectively. In this study, four potentially state-dependent predictors

https://doi.org/10.5194/nhess-2020-120
Preprint. Discussion started: 20 April 2020

(1,000–300 hPa and 200–50 hPa layer thicknesses, surface skin temperature, and total column water vapor) are applied. The variational bias correction (VarBC) scheme is utilized to update the bias correction coefficient variationally with the new observation operator considered in the cost function of 3DVar.

3. Introduction to the case and experimental design

3.1 Typhoon Soudelor

Typhoon Soudelor, that was happened in August, was the 13th typhoon in 2015 and became the second strongest tropical cyclone in this year. At 1200 UTC 30 July 2015, it formed at northwest Pacific Ocean as a tropical storm, located at 13.6° N, 159.2° E, then moved west by north. It upgraded to a strong tropical storm at 2100 UTC 1 August. Afterwards, it went through a process of rapid intensification. It became a typhoon at 0900 UTC 2 August, a strong typhoon at 2100 UTC 2 August, a super typhoon at 0900 UTC 3 August. Then it weakened to a strong typhoon in the morning on August 5. However, it intensified to a super typhoon again at 1200 UTC 7 August with a maximum speed of 52 m/s, moving west by north, and its intensity raised to its second peak. It was reduced to a strong typhoon again at 1800 UTC 7 August. It decreased to a typhoon, entering to Taiwan channel. It landed again as a typhoon at 1410 UTC on the coast of Fujian province, China. Owing to continuous orographic friction, it decreased to a tropical depression. Fig 1 shows the track of Soudelor and different color lines represent typhoon's maximum wind speed. It is

https://doi.org/10.5194/nhess-2020-120
Preprint. Discussion started: 20 April 2020

displayed that after the formation of typhoon, its track is relatively stable. After July 30, its main body moved west by north at a speed of about 20 km/h. Its moving tendency changed slightly within 10 days of its generation. However, its intensity went through a rapid intensification, a weakening, a second intensification, then a continuous weakening till disappearing gradually after landing Chinese mainland. Fig 2 demonstrates the variation of typhoon's intensity from July 31 to August 5. It is shown that typhoon's maximum wind speed increased fast, while its minimum sea level pressure decreased sharply. This was the stage of typhoon's rapid intensification. We choose the date from August 1 to August 3 during its rapid intensification as our research object.

3.2 Experimental design

Two experiments are designed to test the effects of AHI radiance data direct assimilation on the analysis and forecast of Typhoon Soudelor starting from 1800 UTC 1 August to 0000 UTC 3 August. WRF 3.9.1 is employed as the forecast model in our trial. We use Arakawa C grid in the horizon with a 5 km grid distance. Vertically, it has 41 levels with 10 hPa as its top. Model center is (17.5 °N, 140 °E) (Fig 4). Initial condition and lateral boundary are provided by 0.5°×0.5° GFS reanalysis data. The following parameterization schemes are used: WDM6 microphysics scheme (Lim et al., 2010), Grell Devenyi cumulus parameterization scheme (Grell et al., 2002), RRTM (Rapid Radiative Transfer Model) scheme (Mlawer et al., 1997) and Dudhia scheme for longwave and shortwave radiation respectively. Besides, YSU boundary layer scheme (Noh et al., 2003), Noah land surface scheme are included.

The experimental procedures are illustrated by Fig. 3. Firstly, a 6 hour's spin-up conducted at 1800 UTC 1 August before the forecast at 0000 UTC 2 August is used as the background field for the assimilation. The first experiment is assimilating GTS (Global Telecommunications System) conventional data (including aircraft report, ship report, sounding report, satellite cloud wind data, ground station data) only, which is called control experiment (CTNL). Another experiment is configured with AHI radiance data assimilation (AHI_DA). AHI radiance data is assimilated hourly further from 0000 UTC to 0600 UTC on August 2. Afterwards, an 18 hours forecast is launched as the deterministic forecast. The climatological background error (BE) statistics are estimated using the National Meteorological Center (NMC) method. There are 5 control variables applied in this project including U component, V component, full temperature (T), full surface pressure (Ps), and pseudo-relative humidity (RHs). The observation error for each channel is estimated based on the O-B from 0000 UTC on August 1, 2015 to 0000 UTC on August 3, 2015 every 6 hours.

Fig. 4 is the distribution of GTS observation data at the simulated domain at 0000 UTC 2 August. To avoid latent correlation among adjacent observation, we choose 20 km to rarefy AHI observation data.

4. Results

4.1 Minimization iterations

Fig. 5 shows the change of cost function and gradient with the iteration times. There is an obvious exponential decrease curve in Fig 5a, while Fig 5b shows gradient decreases with the increase of iteration times. Taking Fig. 5a as an example, cost function decreases very remarkably in the first 10 iterations. However, after 30 times of iteration, the cost function curve becomes smooth gradually since only in the first iteration, the differences between background field and observation are largest. With continuous iterations, background field goes through continued adjustments. Finally, the cost function tends to reach a stable minimum that represents the point when cost function has its optimal solution. Besides, the gradient in Fig. 5b decreases stably as the number of times of iteration. The exponential decline of the cost function and the change trend of its gradient indicate that the assimilation effect is satisfying. The final iterated analytical field is close to the observation.

4.2 Analytical results of the brightness temperature

Fig. 6 shows the distribution of observed brightness temperature, simulated background brightness temperature, and simulated analytical field brightness temperature of channel 8, 9, and 10 of AHI at 0000 UTC 2 August 2015. Fig. 6a is the distribution of brightness temperature on channel 8 of AHI. The spiral cloud belt and the eye area of Typhoon Soudelor are vividly shown with 49691 data counts. Fig. 6b is a simulated distribution of background brightness temperature of AHI channel 8 by model and it is generated by a 6 hours' deterministic prediction starting at 1800 UTC 1 August 2015. Although typhoon's spiral cloud belt and eye area are clear in the background field, compared to observed distribution of brightness temperature, there also exist some deviations. It can be seen from the background field and the typhoon core area that the overall magnitude of the brightness temperature is higher than the

https://doi.org/10.5194/nhess-2020-120
Preprint. Discussion started: 20 April 2020

observation. This is mainly caused by a weaker simulated typhoon intensity in the background than observation. Fig. 6c is the distribution of brightness temperature after assimilating AHI radiance data. Spiral cloud belt structure of typhoon is clearly displayed and the overall magnitude of the brightness temperature is similar to the observation, indicating that assimilation of AHI radiance data can improve the analysis of temperature and moisture remarkably. Fig. 6d, e, and f are the observed brightness temperature of AHI channel 9, the simulated brightness temperature of background field, and the simulated brightness temperature of analysis field, respectively. We can find a similar phenomenon: compared to observation, a higher background brightness temperature exists, while the simulated background brightness by analytical field fits closer to the observation. Fig. 6g, h, i represent observational brightness temperature, simulated background brightness temperature, and simulated analytical brightness temperature on channel 10, respectively, and they have similar effects as channel 8 and 9. Generally, the brightness temperature distribution of the three channels is different mainly because the three channels have distinct absorptive bands. From the spiral cloud belt region (orange) of the background field, obviously the simulated background brightness temperature of three channels is higher than corresponding observation, while after assimilating AHI radiance data, compared to background brightness temperature, simulated analytical brightness temperature is closer to the observation.

Fig. 6 shows the distribution of observed brightness temperature minus

https://doi.org/10.5194/nhess-2020-120
Preprint. Discussion started: 20 April 2020

background brightness temperature (OMB) and the observed brightness temperature minus analytical brightness temperature (OMA) after the bias correction of AHI radiance data from channel 8, 9, and 10 at 0000 UTC 2 August 2015. Fig. 6a is the distribution of OMB brightness temperature after the bias correction. In the figure, part of typhoon's spiral cloud belt is clearly visible. The brightness temperature in typhoon's core area is low, while the brightness temperature in other areas is high. The mean of observed OMB was -4.65 K, indicating that the background brightness temperature is higher than the observation. Fig. 6b shows that the OMA value of most pixels are below 0.02 K, indicating that the analytical field fitting the observation after analyzing. It can be inferred from Fig. 6a, c, and e that the magnitude in OMB of channel 10 is generally larger than that of channel 9, while that of the OMB of channel 8 is the smallest. This is because the detection height of channel 10 is lower than that of channel 8 and 9, which is most greatly affected by the cloud. Conversely, the weight peak of the channel 8 is the highest, being the channel least affected by the cloud. In general, the analytical brightness temperature match well with the observed brightness temperature of all the three water vapor channels after the assimilation of AHI radiance data.

Fig. 7 illustrates the effect of the bias correction for AHI radiance data at 0000 UTC 2 August 2015. Fig. 7a, d, g are the scatter plots of the observed brightness temperature and the background brightness temperature field before the bias correction. The abscissa represents the observed brightness temperature and the

https://doi.org/10.5194/nhess-2020-120
Preprint. Discussion started: 20 April 2020

ordinate represents the background brightness temperature simulated by CRTM observation operator according to the mode background field. Fig. 7b, e, h are results after bias correction, Fig. 7c, f, i are the scatter plots of observed brightness temperature and analytical brightness temperature after bias correction. From Fig. 7a, before the bias correction, the values from the observation and the background are comparaible, but most of the scatter points are below the diagonal line. This suggests that the observed brightness temperature is higher than the background simulated brightness temperature. From Fig. 7b, after the bias correction, observed warm bias is corrected to some degree. From Fig. 7a, b, after the bias correction, the root mean square error (RMSE) of OMB decreases from 1.864 K to 1.627 K, with the average decreasing from 0.956 K to 0.358 K, proving the validity and rationality of the variational bias correction. Compared to the result of Fig. 7b, the scatters in Fig. 7c are more symmetrical, fitting closely to the diagonal line. The mean and RMSE were also significantly reduced, suggesting that the analytical field is more similar to observation than background field. Channel 9, 10 have a similar result, but with a significantly reduced mean and RMSE, indicating that the background field and analytical field of channel 9, 10 match better with the observation than channel 8 does. Among them the RMSE of channel 10 reaches the minimum. In Fig. 7i, the RMSE of channel 10 analytical field is only 0.234 K.

Fig. 8 shows the observation number, the mean, and the standard deviation of OMB and OMA of assimilation channel 8, 9, and 10 before and after bias correction.

It can be seen from the figure that after quality control, 24057, 24181, 21785 observation data enter the assimilation system in channel 8, 9, and 10, respectively. From the mean value of OMB before the bias correction, the value of the three channels is relatively small, indicating that the simulated brightness temperature of the three channels is close to the actual brightness temperature. The lowest mean of 0.3 K is found in channel 10, indicating that the simulated brightness temperature of channel 10 is closest to the observed brightness temperature. Bias correction effectively corrects the systematic bias and reduces the mean value of observation residuals. After the bias correction, the OMB mean value of the three channels significantly decreases to nearly 0 K. With the bias correction, the simulated brightness temperature is almost the same as the observed brightness temperature. The analysis of the standard deviation of OMB shows that the results are compariable before and after the bias correction, indicating that the bias correction basically does not change the spread of OMB. The standard deviation of OMA decreases by about 80% compared to OMB, indicating that the error distribution is greatly improved after assimilation.

The RMSEs of the simulated brightness temperature by the model before assimilation and assimilation against the observation is also calculated. Fig. 9 shows the above RMSEs during the assimilation time for channels 8, 9, 10. As can be seen from Fig. 9, RMSE decreases after each analysis of the AHI assimilation experiment compared with the previous one. The most significant improvement is from the first

https://doi.org/10.5194/nhess-2020-120
Preprint. Discussion started: 20 April 2020

analysis moment of channel 8, where RMSE of the brightness temperature after assimilation significantly decreases from 1.64 K to 0.46 K, possibly due to the largest observation increment at the first analytical time. The one hour forecast after the analysis basically makes brightness temperature of RMSE increase. Overall, the effect of the analysis of the channel 10 is most significant.

4.3 Analysis of the typhoon structure

Fig. 10 shows the wind field at sea level and the distribution of water vapor at 0000 UTC 2 August 2015. The obvious cyclonic eddy circulation structures in the core area of the typhoon are found in both fields, while the anti-cyclonic circulation exists in the northwest quadrant of the typhoon. The mixing ratio of water vapor in the region where the typhoon is located is very high and the wind field is cyclonic, indicating that the typhoon has a continuous water vapor advection. This is conducive to the enhancement of typhoon. According to the flow field of the control experiment in Fig. 10a, it can be seen that the water vapor convergence in the center of the typhoon region is weak with the low intensity, and the water vapor convergence zone is small. As can be seen from Fig. 10b, after the assimilation of AHI radiance data, the streamlines in the typhoon region become denser, indicating that the cyclonic circulation is strengthened. Compared to the control experiment, the intensity and distribution of the moisture convergence zone after the assimilation of AHI radiance data are also more beneficial to the development of typhoon. This suggests that the assimilation of AHI radiance data is able to significantly improve the large-scale

https://doi.org/10.5194/nhess-2020-120
Preprint. Discussion started: 20 April 2020

environmental field in the simulation region of the typhoon system.

4.4 Track forecast

In order to further evaluate the effect of AHI radiance assimilation, a 18-hour deterministic forecast is launched at the end of two assimilation experiments. As can be seen in Fig. 11a, at the beginning of the forecast, the initial location of the typhoon of the two trials has a large bias. The location of the typhoon in the control experiment has a relative east-southward bias, while the location of the typhoon in AHI_DA trial is relatively close to the observation. During the following 6-hour forecast, the typhoon track predicted by the CTNL continues moving west-south with the environmental wind, while the track simulated by AHI_DA experiment match better with the best track than that of the CTNL. In summary, the track of AHI_DA trial is closest to the observation track during the entire 18-hour deterministic forecast. Fig. 11b is the typhoon track error predicted by the two experiments. At the initial time of prediction, the track errors of CTNL and AHI_DA are significantly different, with magnitude of 63.2km and 16.7km, respectively. During the subsequent 18-hour forecast, the track error of the CTNL gradually increases with the forecast time reaching 232.5km at the end of the forecast. In contrast, the track error of AHI_DA experiment is better controlled within 95 km during the entire 18-hour deterministic prediction process. In general, the average track error of the CTNL is 123.46 km, and the average track error of AHI_DA experiment is 53 km, indicating a significant improvement in the track prediction.

https://doi.org/10.5194/nhess-2020-120
Preprint. Discussion started: 20 April 2020

Fig. 12 discusses the time series of the typhoon intensity from the two experiments with the maximum surface wind speed and minimum sea level pressure (SLP) shown in Fig. 12a and Fig. 12b respectively. It can be seen that the maximum near surface wind speed predicted by the CTNL is much lower than the actual wind speed, mainly because the overall strength of Typhoon Soudelor simulated in the background field of the model is relatively weaker. The maximum near surface wind speed predicted by AHI_DA experiment fit closer to the best track with the maximum difference about 2.6m /s after 12 hours forecast. In, Fig. 12b, the results of the minimum SLP are consistent with Fig. 12a.

5. Conclusion

An interface for AHI data assimilation on the WRFDA system based on the 3DVAR assimilation method was built. Based on the Typhoon Soudelor in 2015, two assimilation experiments for comparison was designed to examine the impact of AHI moisture channel radiance data assimilation on the analysis and prediction of the rapid development stage of typhoon under the condition of clear sky. Following conclusions are obtained:

(1) The AHI imager on the new generation of geostationary meteorological satellite is able to reflect the structure of Typhoon Soudelor very clearly. After a series of pre-procedures such as the quality control, the bias correction, contaminated pixel data is able to effectively be eliminated, ensuring the validity and rationality of the observation data. The bias from the observations are also eliminated from the VarBC

https://doi.org/10.5194/nhess-2020-120
Preprint. Discussion started: 20 April 2020

statistical method, which is able to provide a positive impact on the data assimilation procedure for the typhoon numerical simulation.

(2) Compared with the control experiment with the GTS data assimilation, the 3DVAR assimilation performed with AHI radiance data on top of the GTS data is able to improve the structure of typhoon's core and outer rainband. Also, the position and intensity of typhoon in the background field are able to be corrected.

(3) Compared to the predicted intensity and track of the control experiment and the best track, it is found that the track, maximum wind speed, and minimum sea level pressure from the AHI radiance data assimilation experiment are more similar to the observation than the control experiment for the subsequent 18-hour forecast.

This paper realizes the AHI moisture channel radiance data assimilation under the condition of clear sky. The results of the experiments indicate that AHI data assimilation has a positive effect on the analysis and prediction of typhoon of the rapid development stage of Typhoon Soudelor. Considering the complex influence of underlying surface, only the rapid development stage of typhoon at sea were studied, while the whole generation, development and disappearance stage of typhoon can also be studied in the future. In addition, based on the AHI data of the water vapor channels under the condition of clear sky, only 3DVAR method was adopted. Further improvements under the condition of all sky and hybrid can be obtained in the future.

https://doi.org/10.5194/nhess-2020-120
Preprint. Discussion started: 20 April 2020

Acknowledgments

This research was primarily supported by the Chinese National Natural Science Foundation of China (G41805016, G41805070), the Natural Science Foundation of Jiangsu Province (BK20170940), the Chinese National Key R&D Program of China (2018YFC1506404, 2018YFC1506603), the research project of Heavy Rain and Drought-Flood Disasters in Plateau and Basin Key Laboratory of Sichuan Province in China (SZKT201901, SZKT201904), and the Joint Open Project of KLME & CIC-FEMD, NUIST (KLME201807, KLME201808).

References

Bauer, P., Geer, A.J., Lopez, P., and Salmond, D.: Direct 4D–Var assimilation of all-sky radiance. Part I: Implementation, Quarterly Journal of the Royal Meteorological Society, 136, 1868-1885, 2010.

Bauer, P., Auligné, T., Bell, W., Geer, A., Guidard, V., Heilliette, S., et al: Satellite cloud and precipitation assimilation at operational NWP centres, Quarterly Journal of the Royal Meteorological Society, 137, 1934-1951, 2011.

Bessho, K., Date, K., Hayashi, M., Ikeda, A., Imai, T., Inoue, H., et al.: An introduction to Himawari-8/9—Japan's new-generation geostationary meteorological satellites, Journal of the Meteorological Society of Japan, 94, 151-183, 2016.

Buehner, M., Caya, A., Carrieres, T., and Pogson, L.: Assimilation of SSMIS and

https://doi.org/10.5194/nhess-2020-120
Preprint. Discussion started: 20 April 2020

Natural Hazards and Earth System Sciences
Open Access
EGU
Discussions

ASCAT data and the replacement of highly uncertain estimates in the Environment Canada Regional Ice Prediction System, Quarterly Journal of the Royal Meteorological Society, 142, 562-573, 2016.

Dee, D.P., and Uppala, S.: Variational bias correction of satellite radiance data in the ERA–Interim reanalysis, Quarterly Journal of the Royal Meteorological Society, 135, 1830-1841, 2009.

DeMaria, M., Sampson C.R., Knaff J.A., and Musgrave K.D.: Is tropical cyclone intensity guidance improving? Bulletin of the American Meteorological Society, 95, 387-398, 2014.

Derber, J.C., and Wu, W.S.: The use of TOVS cloud–cleared radiance in the NCEP SSI analysis system, Monthly Weather Review, 126, 2287-2299, 1998.

Di, D., Ai, Y., Li， J., Shi, W., and Lu, N.: Geostationary satellite-based 6.7 μm band best water vapor information layer analysis over the Tibetan Plateau, Journal of Geophysical Research: Atmospheres, 121, 4600-4613, 2016.

Goodman, S.J., Gurka, J., DeMaria, M., Schmit, T.J., Mostek, A., Jedlovec, G., et al.: The GOES-R proving ground: Accelerating user readiness for the next-generation geostationary environmental satellite system, Bulletin of the American Meteorological Society, 93, 1029-1040, 2012.

Grell G.A., Dévényi D.: A generalized approach to parameterizing convection combining ensemble and data assimilation techniques, Geophys. Res. Let., 29, 587-590, 2002.

Hilton, F., Atkinson, N. C., English, S. J., and Eyre, J. R.: Assimilation of IASI at the Met Office and assessment of its impact through observing system experiments, Quarterly Journal of the Royal Meteorological Society, 135, 495-505, 2009.

Jung, J.A., Zapotocny, T.H., Le Marshall, J.F., and Treadon, R.E.: A two-season impact study on NOAA polar-orbiting satellites in the NCEP Global Data Assimilation System, Weather Forecasting, 23, 854-877, 2008.

Kazumori, M.: Satellite radiance assimilation in the JMA operational mesoscale 4DVAR system, Monthly Weather Review, 142, 1361-1381, 2014.

Li, X., and Zou, X.: Bias characterization of CrIS radiances at 399 selected channels with respect to NWP model simulations, Atmospheric Research, 196, 164-181, 2017.

Liu, Z., Schwartz, C.S., Snyder, C., and Ha, S.Y.: Impact of assimilating AMSU-A radiance on forecasts of 2008 Atlantic tropical cyclones initialized with a limited-area ensemble Kalman filter, Monthly Weather Review, 140, 4017-4034, 2012.

Ma, Z., Maddy E.S., Zhang B., Zhu T., and Boukabara S.A.: Impact Assessment of Himawari-8 AHI Data Assimilation in NCEP GDAS/GFS with GSI, J. Atmos. Oceanic Technol., 34, 797-815, 2017.

McNally, A.P., Watts, P.D., Smith, J.A., Engelen, R., Kelly, G.A., Thépaut, J.N., and Matricardi, M.: The assimilation of AIRS radiance data at ECMWF, Quarterly Journal of the Royal Meteorological Society, 132, 935-957, 2006.

https://doi.org/10.5194/nhess-2020-120
Preprint. Discussion started: 20 April 2020

Natural Hazards and Earth System Sciences
Open Access
Discussions

Mlawer E.J., Taubman S.J., Brown P.D., et al.: Radiative transfer for inhomogeneous atmospheres: RRTM, a validated correlated-k model for the longwave, Journal of Geophysical Research Atmospheres, 102: 16663-16682, 1997.

Montmerle, T., Rabier, F., and Fischer, C.: Relative impact of polar–orbiting and geostationary satellite radiance in the Aladin/France numerical weather prediction system, Quarterly Journal of the Royal Meteorological Society, 133, 655-671, 2007.

Noh Y., Cheon W.G., Hong S.Y., et al. Improvement of the K-profile Model for the Planetary Boundary Layer based on Large Eddy Simulation Data, Boundary-Layer Meteorology, 107: 401-427, 2003.

Prunet, P., Thépaut, J.N., Cassé, V., Pailleux, J., Baverez, A., and Cardinali, C.: Strategies for the assimilation of new satellite measurements at Météo–France, Advances in Space Research, 25, 1073-1076, 2000.

Qin, Z., Zou, X., Weng, F.: Evaluating Added Benefits of Assimilating GOES Imager Radiance Data in GSI for Coastal QPFs, Monthly Weather Review, 141, 75-92, 2013.

Rennie, M.P.: The impact of GPS radio occultation assimilation at the Met Office, Quarterly Journal of the Royal Meteorological Society, 136, 116-131, 2010.

Schmit, T.J., Gunshor, M.M., Paul Menzel, W., Gurka, J., Li, J., and Bachmeier, S.: Introducing the next–generation advanced baseline imager (ABI) on GOES-R, Bulletin of the American Meteorological Society, 86, 1079-1096, 2005.

Schmit, T.J., Li, J., Li, J., Feltz, W.F., Gurka, J.J., Goldberg, M.D., and Schrab, K.J.: The GOES-R Advanced Baseline Imager and the continuation of current sounder products, Journal of Applied Meteorology and Climatology, 47, 2696-2711, 2008.

Schmit, T.J., Griffith, P., Gunshor, M.M., Daniels, J.M., Goodman, S.J., and Lebair, W.J.: A closer look at the ABI on the GOES-R series, Bulletin of the American Meteorological Society, 98, 681-698, 2017.

Shen, F., and Min, J.: Assimilating AMSU-A radiance data with the WRF hybrid En3DVAR system for track predictions of Typhoon Megi (2010), Advances in Atmospheric Sciences, 32, 1231-1243, 2015.

Stengel, M., Undén, P., Lindskog, M., Dahlgren, P., Gustafsson, N., and Bennartz, R.: Assimilation of SEVIRI infrared radiance with HIRLAM 4D-Var, Quarterly Journal of the Royal Meteorological Society, 135, 2100-2109, 2009.

Wang, Y., Liu, Z., Yang, S., Min, J., Chen, L., Chen, Y., and Zhang, T.: Added value of assimilating Himawari-8 AHI water vapor radiances on analyses and forecasts for “7.19” severe storm over north China, Journal of Geophysical Research: Atmospheres, 123, 3374-3394, 2018.

Xu, D., Liu, Z., Huang, X., Min, J., and Wang, H.: Impact of assimilation IASI radiances on forecasts of two tropical cyclones, Meteorology and Atmospheric Physics, 122, 1-18, 2013.

Zapotocny, T.H., Jung, J.A., Le Marshall, J.F., and Treadon, R.E.: A two–season impact study of satellite and in situ data in the NCEP Global Data Assimilation

System, Weather Forecasting, 22, 887-909, 2007.

Zhu, Y., Derber, J., Collard, A., Dee, D., Treadon, R., Gayno, G., and Jung, J.A.: Enhanced radiance bias correction in the National Centers for Environmental Prediction's Gridpoint Statistical Interpolation data assimilation system, Quarterly Journal of the Royal Meteorological Societ, 140, 1479-1492, 2014.

Zou, X., Qin, Z., and Weng, F.: Improved coastal precipitation forecasts with direct assimilation of GOES-11/12 imager radiance, Monthly Weather Review, 139, 3711-3729, 2011.

Zou, X., Qin Z., and Zheng Y.: Improved tropical storm forecasts with GOES-13/15 imager radiance assimilation and asymmetric vortex initialization in HWRF, Monthly Weather Review, 143, 2485-2505, 2015.

https://doi.org/10.5194/nhess-2020-120
Preprint. Discussion started: 20 April 2020

Natural Hazards and Earth System Sciences
Open Access
Discussions

List of Figures

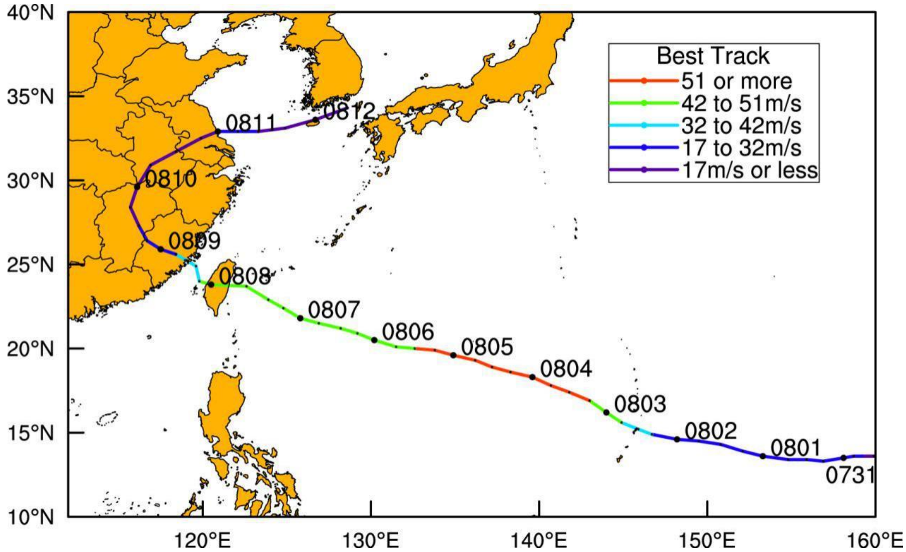

Fig.1 The track of Typhoon "Soudelor" in August 2015. Different colors represent intensity changes.

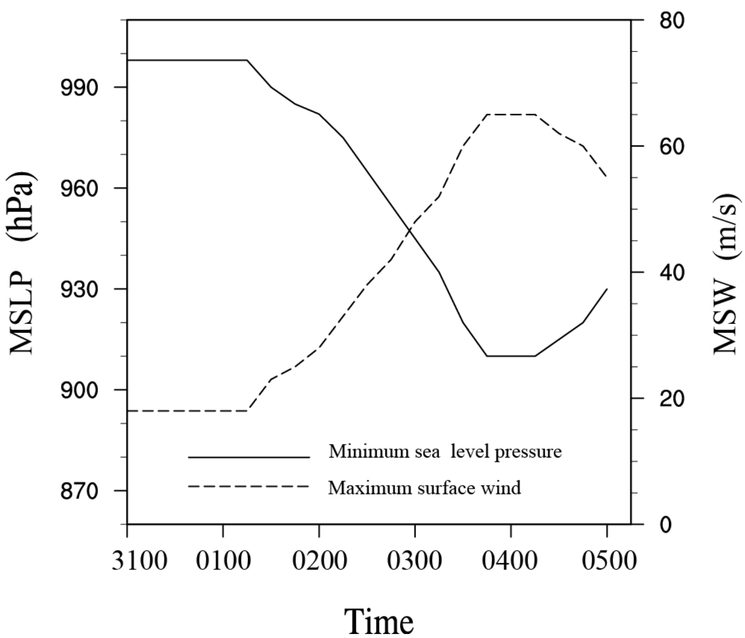

https://doi.org/10.5194/nhess-2020-120
Preprint. Discussion started: 20 April 2020

Fig.2 The time series of the minimum sea level pressure (solid line, unit: hPa) and the maximum wind speed (dash line, unit: m/s) from July 31, 2015 to August 5, 2015.

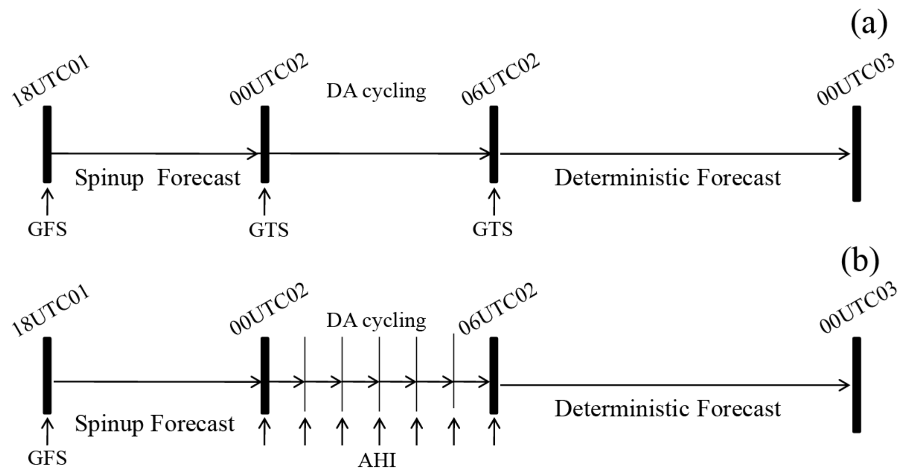

Fig. 3 The flow chart of experiments: (a) represents CTNL while (b) represents AHI_DA

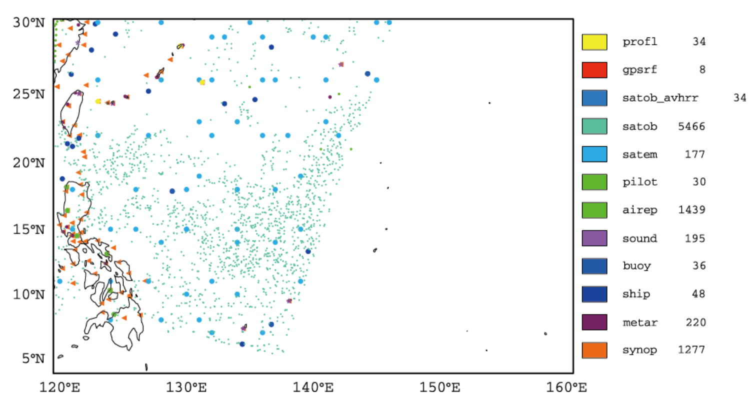

Fig. 4 Distribution of GTS in the simulated area at 0000 UTC 2 August 2015. On the right side of the map is the name of observation data and the number of observations.

https://doi.org/10.5194/nhess-2020-120
Preprint. Discussion started: 20 April 2020

Natural Hazards and Earth System Sciences
Open Access
Discussions

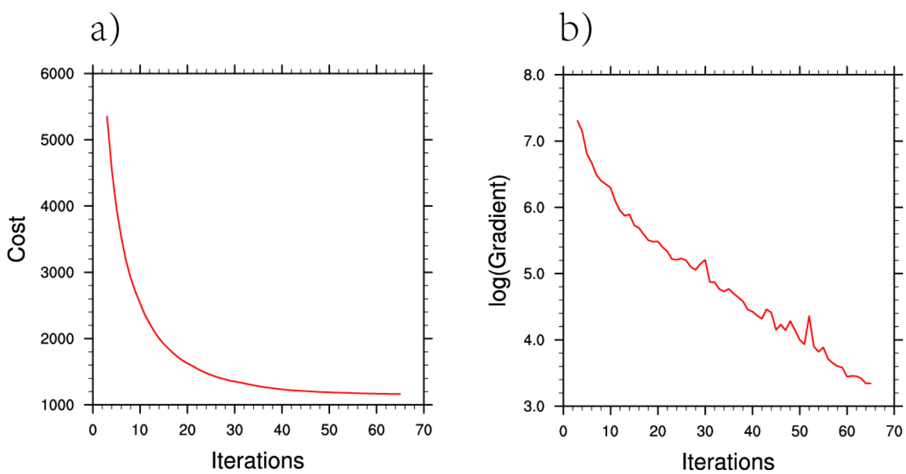

Fig. 5 (a) is a schematic diagram of the change of cost function with the number of iterations, and (b) is a schematic diagram of the change of gradient with the number of iterations.

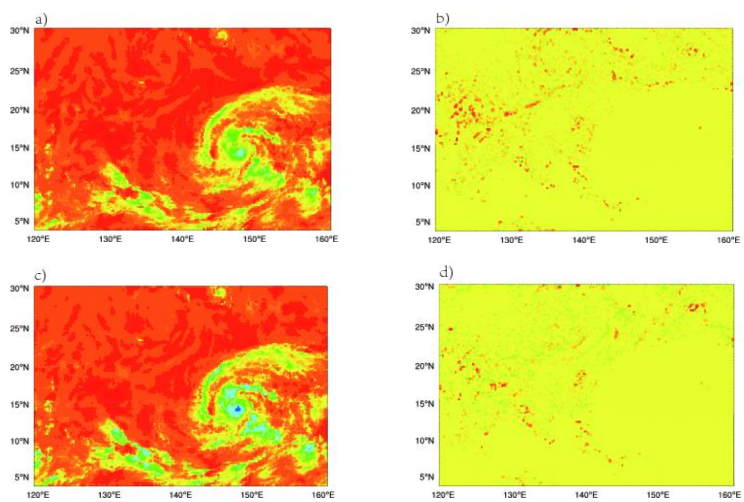

https://doi.org/10.5194/nhess-2020-120
Preprint. Discussion started: 20 April 2020

Natural Hazards and Earth System Sciences
Open Access
Discussions

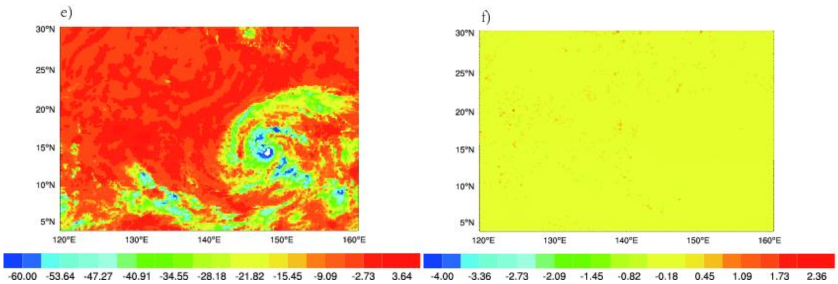

Fig. 6 (a, c, and e) represent OMB (unit: K) after bias correction for channel 8, 9, and 10, respectively; (b, d, and f) represent OMA (unit: K) after bias correction for channel 8, 9, and 10, respectively at 0000 UTC 2 August 2015.

https://doi.org/10.5194/nhess-2020-120
Preprint. Discussion started: 20 April 2020

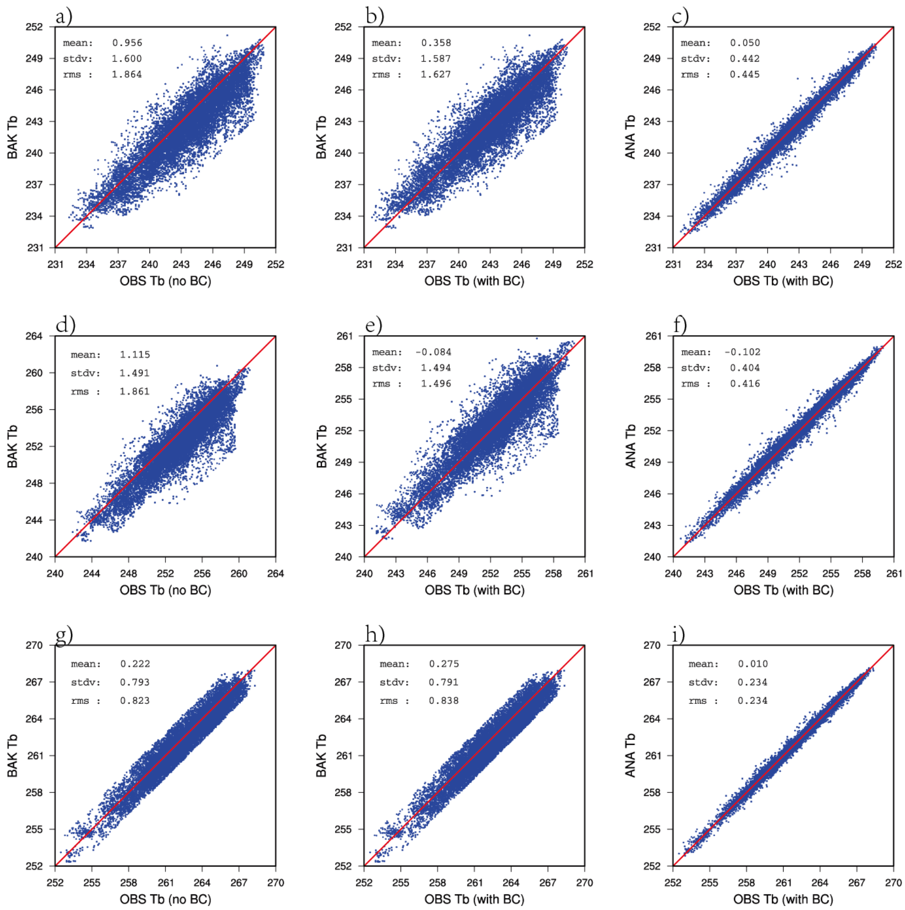

Fig. 7 Scatter plots of (a, d and g) the observed and background brightness temperature before the bias correction of channel 8, 9 and 10. Scatter plots of (b, e and h) the observed and background brightness temperature after the bias correction of channel 8, 9 and 10. Scatter plots of (c, f and i) the observed and analyzed brightness temperature after the bias correction of channel 8, 9 and 10.

https://doi.org/10.5194/nhess-2020-120
Preprint. Discussion started: 20 April 2020

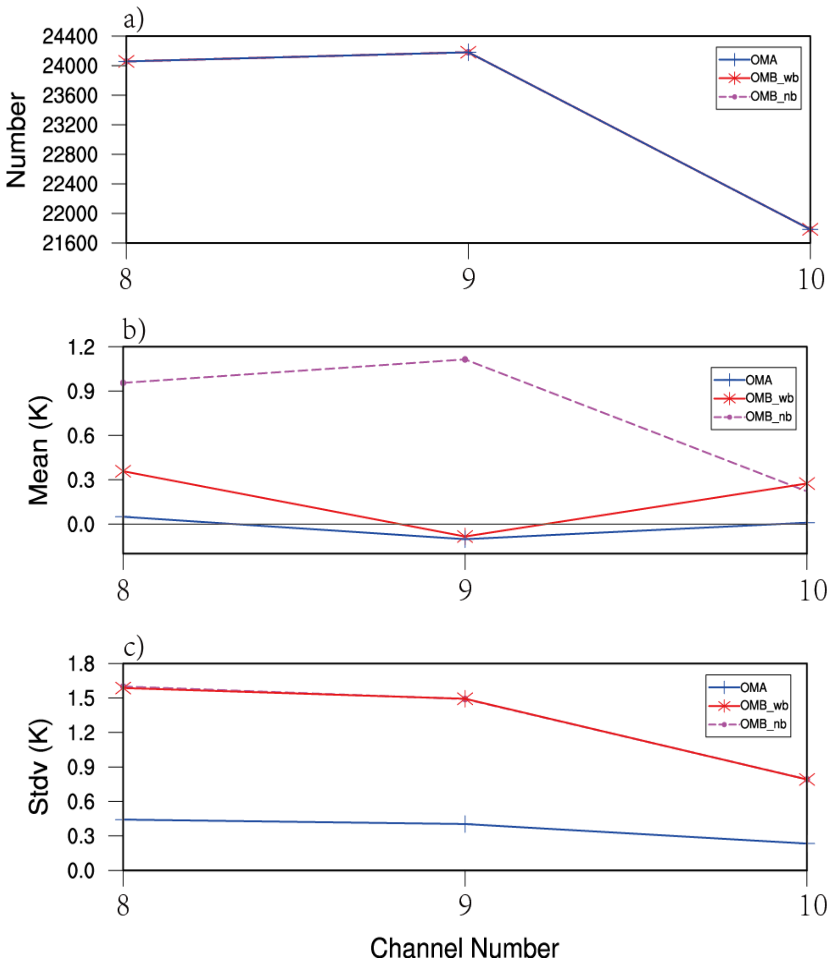

Fig. 8 Number of (a) observations, (b) mean (unit: K), and (c) standard deviations (unit: K) of OMB and OMA before and after bias correction for water vapor channel 8-10 assimilation (OMB_nb: OMB without bias correction; OMB_wb: OMB with bias correction).

https://doi.org/10.5194/nhess-2020-120
Preprint. Discussion started: 20 April 2020

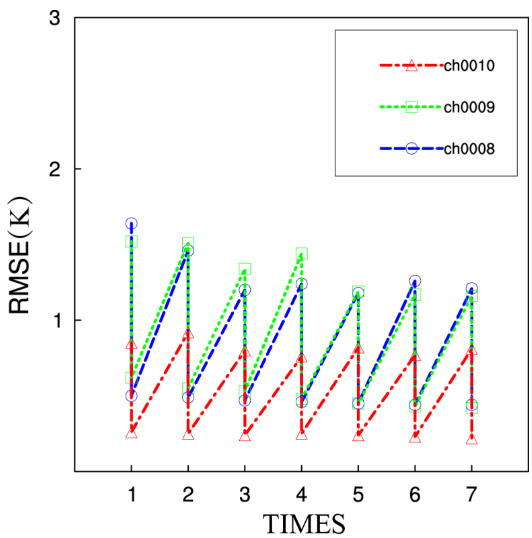

Fig. 9 Time series of the RMSE for the brightness temperature (unit: K) with assimilation times before and after the data assimilation.

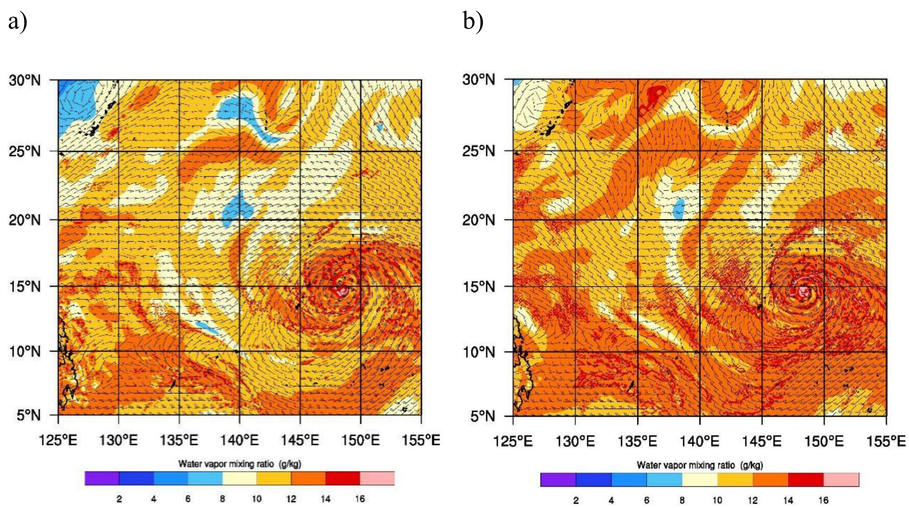

Fig. 10 The surface wind speed (vectors, unit: m/s) and water vapor (colored, unit: g/kg) for (a) CTNL; (b) AHI_DA at 0000 UTC 2 August 2015.

https://doi.org/10.5194/nhess-2020-120
Preprint. Discussion started: 20 April 2020

Natural Hazards and Earth System Sciences
Open Access
Discussions

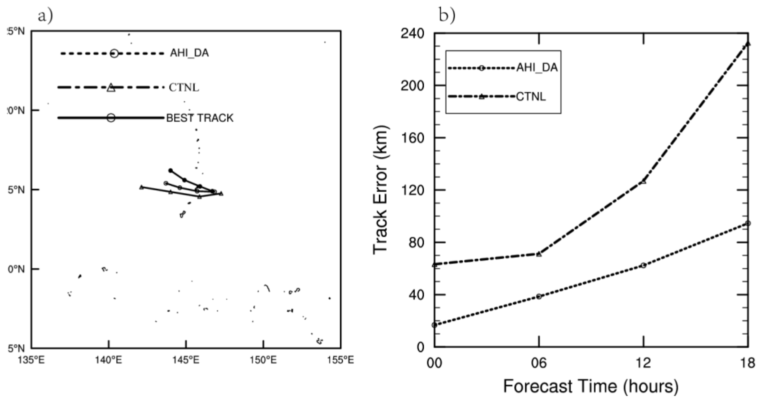

Fig. 11 The 18-hour (a) predicted tracks and the best track, (b) track errors (unit: m/s) of Soulder from 0600 UTC 2 to 0000 UTC 3 August 2015.

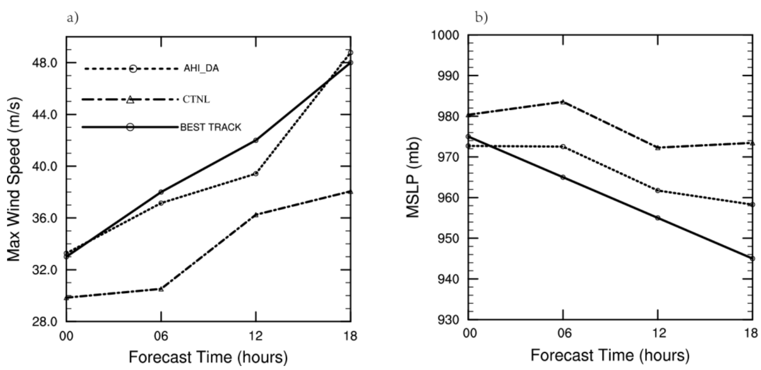

Fig.12 The 18-hour predicted (a) maximum surface wind speed (unit: m/s)，(b) minimum SLP (unit: hPa) of Soulder from 0600 UTC 2 to 0000 UTC 3 August 2015.